Journal of Materials Chemistry A

RSC Publishing

COMMUNICATION

View Article Online
View Journal | View Issue

Effects of oxygen vacancies on the electrochemical performance of tin oxide†

Cite this: *J. Mater. Chem. A*, 2013, **1**, 1536

Received 7th November 2012
Accepted 3rd December 2012

DOI: 10.1039/c2ta01012g

www.rsc.org/MaterialsA

Na Li,[ab] Kui Du,[a] Gang Liu,[a] Yingpeng Xie,[a] Guangmin Zhou,[a] Jing Zhu,[c] Feng Li*[a] and Hui-Ming Cheng[a]

Using an aberration-corrected transmission electron microscope, we observed the oxygen vacancies, profiled the concentration in the $SnO_{2-\delta}$ nanocrystals on an atomic scale, and estimated the amount of oxygen vacancies to be *ca.* 3.3 atom%. The $SnO_{2-\delta}$ nanocrystals show much improved initial Coulombic efficiency, rate capability and specific capacity compared with stoichiometric SnO_2 when used as an anode material for lithium ion batteries.

Defects often dominate the physical and chemical properties of semiconducting materials. Oxygen vacancies in oxides are particularly important because they are generally electron donors. Therefore, oxygen vacancies play an important role in a wide range of applications, such as photocatalysis, heterogeneous catalysis, field-effect devices and sanitary disinfection.[1–4] However, in the field of lithium ion batteries (LIBs), the relationship between oxygen vacancies and the electrochemical properties of electrode materials has rarely been studied,[5,6] and little is known about how oxygen vacancies affect the electrochemical properties. On the other hand, exploring measurement methods for oxygen vacancy concentrations on an atomic scale is also important. It is necessary to understand the structure of defects and how their electronic properties are influenced by deviations of the local oxygen concentration from stoichiometry. Until now, the observation of oxygen vacancy concentrations directly has been challenging. The available structural characterization techniques for studying oxygen in oxides, X-ray and neutron scattering and electron crystallography, do not allow defects to be studied. Referring to the microscopic techniques, the contrast based on the high-angle scattering of electrons (*Z*-contrast) in scanning transmission electron microscopy does not allow oxygen to be imaged because it is confined to elements with a high value of the nuclear charge *Z*.[7] In conventional high-resolution transmission electron microscopy (HRTEM), it is possible to image the cation columns projected along the viewing direction under suitable conditions. The reason is that the cations have a high nuclear charge and their scattering power is high, resulting in strong phase contrast. In comparison, it is difficult to image an oxygen sublattice due to the relatively low scattering power. Jia *et al.*[8] first imaged all types of atomic columns in thin films of $SrTiO_3$ and $YBa_2Cu_3O_7$ using an imaging mode based on adjusting the spherical-aberration coefficient of the objective lens to a negative value in a transmission electron microscope (TEM). This method opens a way to the microscopic study of individual vacancies, and the use of this method for other films has been reported. However, it remains a challenge and there are no related reports on the measurements of oxygen vacancy concentrations in nanoparticles.

In this work, we explore the effect of oxygen vacancies on the electrochemical properties of SnO_2 which is a very popular high-capacity anode for LIBs. Importantly, we profile the oxygen vacancy concentration in $SnO_{2-\delta}$ nanoparticles on the atomic scale using an aberration-corrected TEM.

By using tin(II) chloride as a precursor, Sn^{2+} will not be completely oxidized to Sn^{4+} under a low temperature hydrothermal process, and thus the oxygen vacancy detected is dominantly derived from Sn^{2+}. Fig. S1† reveals the high-resolution XPS spectra of $SnO_{2-\delta}$ and SnO_2. The Sn $3d_{5/2}$ peak for $SnO_{2-\delta}$ consists of two different chemically shifted components (Fig. S1a†). The components at 486.7 eV and 487.5 eV are ascribed to Sn^{2+} and Sn^{4+}, while no Sn^{2+} was detected from the Sn $3d_{5/2}$ peak for the SnO_2 free of oxygen vacancy (Fig. S1b†). Observation with TEM clearly shows that both $SnO_{2-\delta}$ and SnO_2 crystals have a similar size of around 5 nm (Fig. S2†). SnO_2 has a rutile structure (space group $P4_2/mnm$) with lattice parameters $a_0 = 4.738$ Å and $c_0 = 3.1865$ Å. Its low index surface (110) (Fig. 1a) is the most thermodynamically stable. The lattice fringes with a spacing of 0.33 nm in Fig. 1b correspond to the most stable and frequently observed rutile SnO_2 (110). The broad diffraction peaks of $SnO_{2-\delta}$ and SnO_2 suggest a small crystallite size

[a]*Shenyang National Laboratory for Materials Science, Institute of Metal Research, Chinese Academy of Sciences, 72 Wenhua Road, Shenyang 110016, China. E-mail: fli@imr.ac.cn; Fax: +86 24 23903126; Tel: +86 24 23971472*

[b]*Department of Materials Science & Engineering, School of Chemistry and Materials Science, University of Science and Technology of China, Hefei 230026, China*

[c]*Beijing National Center for Electron Microscopy, Tsinghua University, Beijing 100084, China*

† Electronic supplementary information (ESI) available: Sample preparation, performance tests, TEM images. See DOI: 10.1039/c2ta01012g

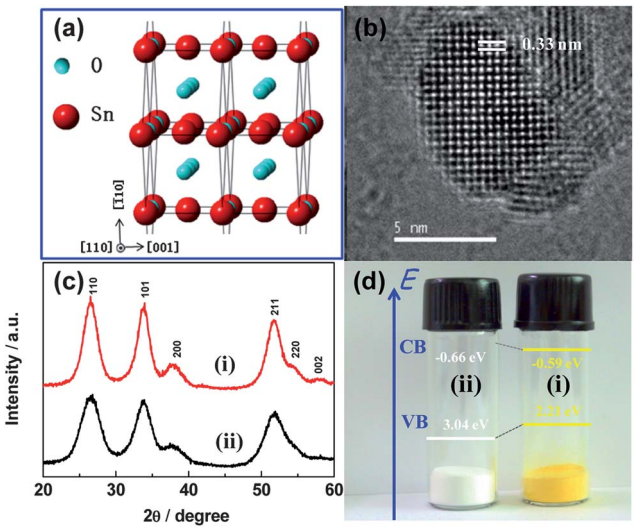

Fig. 1 (a) SnO_2 with a rutile structure projected along the [110] axis showing separate O and Sn columns; (b) HRTEM image of a single SnO_2-particle; (c) XRD patterns of (i) $SnO_{2-\delta}$ and (ii) SnO_2 particles; (d) photographs of (i) $SnO_{2-\delta}$ (yellow) and (ii) SnO_2 (white) powders. Conduction band is denoted as CB and valence band as VB.

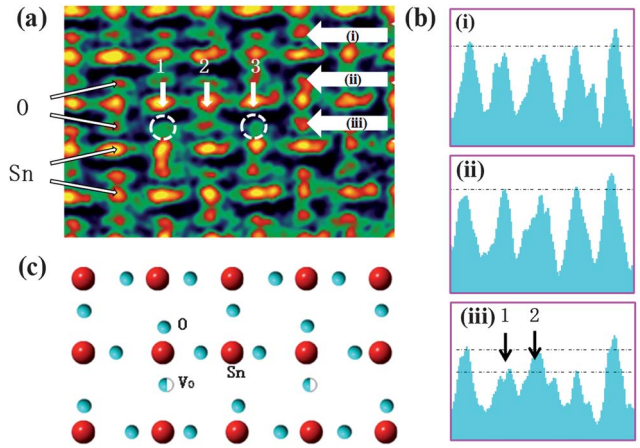

Fig. 2 (a) HRTEM image of a rutile $SnO_{2-\delta}$ particle along the [110] zone axis, which reveals alternating oxygen and tin atoms (arrows) and the deficiency of O columns. Contrast at the centre of the O columns is indiscernible, indicated by a dashed circle; (b) normalized intensity variations of columns of O atoms according to arrows (i), (ii) and (iii) in (a). The intensities at positions 1 and 2 are compared, where the intensity ratio of I_1 and I_2 is 0.75; (c) crystal structure obtained by removing oxygen atoms in a stoichiometric SnO_2 (110) surface.

(Fig. 1c). Using the Scherrer equation, the crystal sizes of the $SnO_{2-\delta}$ and SnO_2 nanoparticles were around 5 nm, which are consistent with TEM observations. In $SnO_{2-\delta}$, oxygen vacancies are formed to keep a balanced charge and the resulting localized states are located below the bottom edge of the conduction band. The band gap narrowing behaviour due to oxygen vacancies was clearly apparent from both the optical absorption study and first-principles calculations. This is also shown by the apparent colour change of the powder from white (left bottle: SnO_2) to yellow (right bottle: $SnO_{2-\delta}$) (see Fig. 1d).

Addition of a spherical-aberration corrector to a TEM dramatically improves its spatial resolution, and makes it possible to discern sub-Angstrom details. A wide spectrum of defective structures in various materials has been observed by using aberration-corrected TEM.[9,10] Aberration-corrected TEM images not only reveal individual columns of atoms projected in the beam direction but also provide direct evidence of changes in the chemical composition in individual particles of SnO_2. Fig. 2a shows the HRTEM image of a rutile $SnO_{2-\delta}$ particle along the [110] zone axis, in which O and Sn sites in rutile-structured SnO_2 are seen on an atomic scale. As shown in Fig. 2b, the intensity profiles going through O atom columns along arrows (i), (ii) and (iii) can be assumed to be proportional to the number of atoms in the column along the beam direction. Interestingly, we find that the diffracted intensity of O columns is not uniform in (iii). The intensity of O columns at positions 1 and 3, indicated by a dashed circle, is also weaker than that in the neighbouring O columns (Fig. 2a). It is reasonable to suggest that the regions with a lower diffracted intensity correspond to those with fewer atoms, and the intensity ratio may represent the amounts of O atoms and vacancies. The lower intensity at position 1 than at position 2 in the HRTEM image, with $I_1/I_2 = 0.75$, indicates that the occupancy of the oxygen columns at position 1 is 75% of the stoichiometric value. This is quantitatively shown by the intensity trace in Fig. 2b (iii). Therefore, this analysis estimates that the amount of oxygen vacancies in $SnO_{2-\delta}$ was roughly *ca.* 3.3 atom%. Because a lower intensity corresponds to columns near the central region of the image, this indicates that the effect of thickness change associated with particle shape can be neglected.

This elucidation of the electronic band alignments supports the assumption of oxygen vacancies. The combination of UV-visible absorption spectra with XPS valence band spectra for $SnO_{2-\delta}$ and SnO_2 nanoparticles was used to determine the electronic band alignments. As shown in Fig. 3a, in contrast to SnO_2, the intrinsic absorption edge of the $SnO_{2-\delta}$ has a red shift. The derived bandgaps from the plots of transformed Kubelka–Munk function *vs.* the energy of light are 3.7 and 2.8 eV for the SnO_2 and $SnO_{2-\delta}$ particles, respectively. The bandgap of the $SnO_{2-\delta}$ particles is apparently smaller than that of SnO_2. The bandgap difference between the two

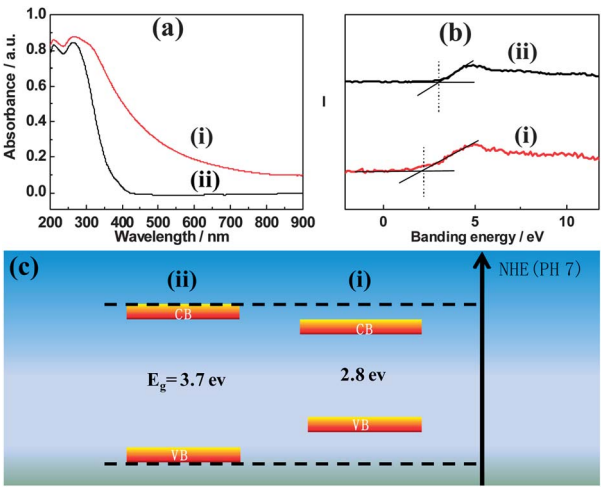

Fig. 3 (a) UV-visible absorption spectra; (b) XPS valence band spectra; and (c) schematic of electronic band alignments of (i) $SnO_{2-\delta}$ and (ii) SnO_2.

samples is inferred to be due to a high percentage of oxygen vacancies in the $SnO_{2-\delta}$. According to the valence band (VB) spectra in Fig. 3b, the VB maxima of SnO_2 and $SnO_{2-\delta}$ nanoparticles are at 3.04 eV and 2.21 eV, respectively, which is consistent with the calculated density of states of tin oxide films along the [110] direction with different numbers of oxygen vacancies.[11] The band-to-band visible light excitation suggests the distribution of oxygen vacancies in the whole particles but only within a subsurface region with very limited depth. On the other hand, the bandgap narrowing behavior due to oxygen vacancies was clearly evidenced from the optical absorption study, which was also shown by the apparent color change of the powders in Fig. 1d.

In a SnO_2-based anode electrode for LIBs, two principal electrochemical processes occur:

$$SnO_2 + 4Li^+ + 4e^- \rightarrow Sn + 2Li_2O \quad (1)$$

$$Sn + xLi^+ + xe^- \leftrightarrow Li_xSn\ (0 \le x \le 4.4) \quad (2)$$

The low initial Coulombic efficiency of SnO_2 is attributed to the formation of a solid electrolyte interphase (SEI) layer and the formation of electrochemically inactive Li_2O. Because the formation of electrochemically inactive Li_2O is of a fundamental electrochemical origin, its mitigation is quite difficult. However, with respect to the reference SnO_2, the $SnO_{2-\delta}$ exhibits a better initial Coulombic efficiency because the oxygen vacancies enable it to accommodate the formation of Li_2O. The anodic performance of $SnO_{2-\delta}$ and SnO_2 with a similar morphology and structure (Fig. S2 and 3†) was tested in a potential range of 0.05 to 2 V (*versus* Li/Li^+). The $SnO_{2-\delta}$ shows a higher initial Coulombic efficiency (64.7%) than that of the SnO_2 (54.6%) and other reports,[12–15] as shown in Fig. 4a. The rational reason for this higher initial Coulombic efficiency is considered to be oxygen vacancies, as described in eqn (3).

$$SnO_{2-\delta} + 2(2-\delta)Li^+ + 2(2-\delta)e^- \rightarrow Sn + (2-\delta)Li_2O \quad (3)$$

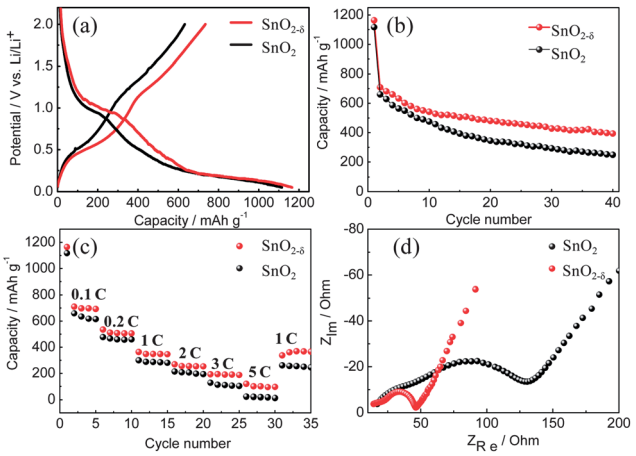

Fig. 4 (a) Charge–discharge curves and (b) cycling performance of the $SnO_{2-\delta}$ and SnO_2 electrodes at 0.1 C (79 mA g^{-1}); (c) comparison of the discharge capacity of the $SnO_{2-\delta}$ and SnO_2 electrodes at different rates; and (d) impedance of coin cells using $SnO_{2-\delta}$ and SnO_2 as electrode materials.

Fig. 4b shows the changes in discharge capacity *versus* cycle number for the $SnO_{2-\delta}$ and SnO_2 electrodes at 0.1 C. It can be easily seen that the $SnO_{2-\delta}$ material exhibits a high discharge capacity of 399 mA h g^{-1} after 40 cycles. Such good reversibility results from the optimization of the nanostructure, which is less than 5 nm in size, thus enabling improved dynamics for both electron and Li^+ transport as well as a high electrode–electrolyte contact area. Fig. 4c shows the rate capability of the SnO_2 and $SnO_{2-\delta}$ electrodes. With respect to the SnO_2, the discharge capacity of $SnO_{2-\delta}$ is substantially increased at all charge–discharge rates from 0.1 C to 5 C. For example, the discharge capacity of $SnO_{2-\delta}$ at 5 C is 101 mA h g^{-1}, 6.5 times higher than that of the SnO_2. The better rate capability of the $SnO_{2-\delta}$ anode is due to oxygen vacancies and its nanostructure that provide the following benefits: (1) the oxygen vacancies provide improved electronic conductivity during the electrochemical process by accommodating the formation of insulated Li_2O. Fig. 4d compares the Nyquist plots of the $SnO_{2-\delta}$ and SnO_2 electrodes. Apparently, the $SnO_{2-\delta}$ electrode shows a much lower resistance than the SnO_2 electrode (49 *vs.* 115 Ω). The conductivity of $SnO_{2-\delta}$ powders was increased by around 1 order of magnitude, showing $\approx 2.3 \times 10^{-6}$ S cm^{-1}, by inducing oxygen vacancy into stoichiometric SnO_2 ($\approx 4.9 \times 10^{-7}$ S cm^{-1}). (2) The nanoparticles prevent coarsening of Sn particles (transformed from SnO_2) in the subsequent cycling. The mode of formation of metallic tin from SnO_2 is an important factor for the rate ability, and Sn particles with a small size enable a fast charge rate of the battery system. Wang *et al.*[16] pointed out the spatial relationship between Sn and Li_2O in the electrochemical reaction, and direct observation indicates that the coarsening of Sn can be minimized by using nanoscale SnO_2 as starting particles.

Conclusion

By using an aberration-corrected TEM, we observed oxygen vacancies and profiled their concentrations in $SnO_{2-\delta}$ nanocrystals on an atomic scale. As an anode material for LIBs, $SnO_{2-\delta}$ shows improved initial Coulombic efficiency, rate capability and charge/discharge capacity compared with stoichiometric SnO_2. The effect of the oxygen vacancy concentrations on the electrochemical properties of SnO_2 or other electrode materials will be further studied.

Experimental section

Sample preparation

Synthesis of $SnO_{2-\delta}$ nanoparticles. In a typical experiment, 1 mmol of tin dichloride dihydrate ($SnCl_2 \cdot 2H_2O$) was added to 40 ml mixed solvent consisting of ethanol and de-ionized water in a 1 : 1 volume ratio to reach a tin(II) concentration of 25 mM. The white turbid suspension obtained was magnetically stirred for 1 h before being transferred to a Teflon-lined stainless steel autoclave and then heated in an electric oven at 120 °C for 6 h. A yellow product was obtained after centrifugation and dried at 50 °C for 24 h.

Synthesis of SnO_2 nanoparticles. The procedure was the same as that for the $SnO_{2-\delta}$ nanoparticles except for using $SnCl_4 \cdot 5H_2O$ as the tin source to replace $SnCl_2 \cdot 2H_2O$. After the solvothermal reaction, a white product was obtained.

Characterization

X-ray diffraction (XRD) patterns of the samples were recorded on a Rigaku diffractometer using Cu Kα irradiation. Scanning electron microscope and TEM images were obtained on a Nova NanoSEM 430 and Tecnai F20, respectively. High resolution TEM images were obtained on a Titan 80-300 aberration-corrected TEM. In this study, the diffracted intensity of atoms is proportional to the number of atoms because of the validity of the weak-phase object approximation in our nanoparticles. Chemical compositions and valence-band spectra of SnO_2 were analyzed by X-ray photoelectron spectroscopy (ThermoEscalab 250, monochromatic Al Ka X-ray source). All binding energies were referenced to the C 1s peak (284.6 eV) arising from adventitious carbon. The optical absorbance spectra of the samples were recorded in a UV/Vis spectrophotometer (JASCO-550).

Conductivity measurements

For conductivity measurements, SnO_2 and $SnO_{2-\delta}$ powders were pressed by cold isostatic pressing with $\approx$10 MPa for 5 min to make pellets (1.15 mm in thickness and 10 mm in diameter). For measuring their *I–V* curves, two probes were used to connect to a Keithley 4200-SCS semiconductor characterization system.

Electrochemical measurements

The electrochemical properties of $SnO_{2-\delta}$ and SnO_2 as anode materials in LIBs were evaluated by a galvanostatic charge/discharge technique. The working electrodes were prepared by mixing $SnO_{2-\delta}$ and SnO_2, carbon black (Super-P), and poly(vinyl difluoride) (PVDF) with a weight ratio of 80 : 10 : 10 and pasted onto a pure copper foil, and then pressed and dried under vacuum at 120 °C for 12 h. Coin cells were assembled in an argon-filled glove box, with metallic lithium as the counter/reference electrode, 1 M $LiPF_6$ in ethylene carbonate (EC)–dimethyl carbonate (DMC) (1 : 1 vol) as the electrolyte, and Celgard 2400 polypropylene as the separator. The electrochemical tests were performed between 0.05 and 2 V *vs.* Li^+/Li and the C-rate currents used were calculated based on an SnO_2 theoretical capacity of 790 mA h g^{-1}.

Acknowledgements

This work was supported by Ministry of Science and Technology of China (no. 2011CB932604) and National Science Foundation of China (no. 50921004 and 51172239). The aberration-corrected transmission electron microscope experiments were carried out using the facility of the Beijing National Center for Electron Microscopy.

Notes and references

1 G. Liu, *et al.*, *J. Phys. Chem. C*, 2009, **113**, 21784.
2 M. Haruta, *et al.*, *J. Catal.*, 1989, **115**, 301.
3 C. H. Ahn, J.-M. Triscone and J. Mannhart, *Nature*, 2004, **424**, 1015.
4 A. Heller, *Acc. Chem. Res.*, 1995, **28**, 503.
5 J. Y. Luo, L. J. Chen, Y. Y. Zhao, P. He and Y. Y. Xia, *J. Power Sources*, 2009, **194**, 1075.
6 J. Y. Shin, J. H. Joo, D. Samuelis and J. Maier, *Chem. Mater.*, 2012, **24**, 543.
7 M. Kim, *et al.*, *Phys. Rev. Lett.*, 2001, **86**, 4056.
8 C. L. Jia, M. Lentzen and K. Urban, *Science*, 2003, **299**, 870.
9 K. W. Urban, *Science*, 2008, **321**, 506.
10 D. A. Muller, N. Nakagawa, A. Ohtomo, J. L. Grazul and H. Y. Hwang, *Nature*, 2004, **430**, 657.
11 H. T. Chen, S. J. Xiong, X. L. Wu, J. Zhu and J. C. Shen, *Nano Lett.*, 2009, **9**, 1926.
12 M. S. Park, G. X. Wang, Y. M. Kang, D. Wexler, S. X. Dou and H. K. Liu, *Angew. Chem., Int. Ed.*, 2007, **46**, 750.
13 J. Fan, T. Wang, C. Yu, B. Tu, Z. Jiang and D. Zhao, *Adv. Mater.*, 2004, **16**, 1432.
14 A. S. Yu and R. Frech, *J. Power Sources*, 2002, **104**, 97.
15 M. S. Park, G. X. Wang, Y. M. Kang, S. Y. Kim, H. K. Liu and S. X. Dou, *Electrochem. Commun.*, 2007, **9**, 71.
16 C. M. Wang, *et al.*, *Nano Lett.*, 2011, **11**, 1874.